IMPERIAL COLLEGE LONDON

Department of Mechanical Engineering

ME4 Individual Project

Modelling and Understanding of the Localised Tip Steering of Soft everting robots

Project Final Report

Yi Lu

June 4, 2025

Supervisor: Ferdinando Rodriguez y Baena

Associate Supervisor: Jialei Shi

Number of pages: 40

IMPERIAL

Abstract

Soft everting robots, also known as vine robots. These robots can achieve growth by everting materials at the robots' tip. As such, they offer unique advantages in navigating constrained and tortuous environments. Understanding and modelling the steering of these robots are challenging. This study investigates the steering performance of a soft everting robot equipped with a pneumatic steerable tip, focusing on the influence of key design parameters. Finite element analysis is used to simulate the robot's steering performance under various growth and steering pressures, and investigate design parameters like manipulator dimension, manipulator material, and fabric strength. To validate the developed finite element model and address its limitations, experimental characterisation is carried out to investigate the fabric characteristics as another design parameter, where the effect of the fabric thickness and the fabric contraction ratio under pressurization is explored. The findings offer valuable insights for designing pneumatically driven tip-steering mechanisms in soft everting robots, particularly for medical applications, where careful selection of materials and dimensions is critical.

Contents

1 Introduction

1.1 Background

Typically, robots are designed with rigid configurations. Although they can perform most tasks, they lack the flexibility to cope with unfamiliar and unpredictable situations when facing a narrow or cluttered environment. To meet this need, soft robots are developed to fit in and operate in all these narrow environments. A unique type of soft robot is known as the soft-everting robot, which is specifically designed to reach and explore those tortuous environments that are inaccessible to classic rigid robots.

Soft-everting robots, also known as vine robots, consist of a cylindrical sleeve of thin flexible material inverted into itself. They feature a tubular structure that grows at the tip by unfolding and rolling out stored material through internal pressurization. In this way, these robots do not need to slide relative to their surroundings. Therefore, they are effectively frictionless with respect to their surroundings and are able to navigate unmapped environments.

This project studies a specific novel soft everting robot used for colonoscopy, which is a medical procedure that examines the inside of the colon for abnormalities like polyps or cancer. This robot features a tube with stretchable fabric. During operation, the fabric is pressurized under a certain growth pressure, as shown in Figure 1. With one end fixed, the inflation pulls the fabric through the body to the tip, causing it to evert and roll onto the outer surface. In this way, the length of the vine robot increases, allowing it to move in restricted environments by growing to an arbitrary length [1].

Controlling the path of a soft everting robot is essential for its navigation, with steering being one of the biggest challenges. Typically, the steering of soft everting robots is achieved by different types of actuators, including tendons, pouch motors, and artificial muscles. For this specific type, localized steerable tip actuation is implemented to steer the robot, which is the focus of this study.

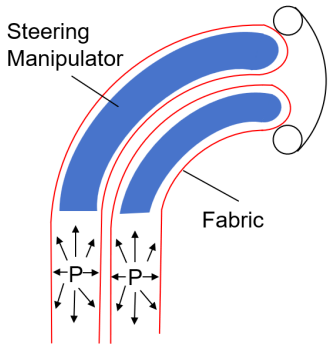

Figure 1: Working mechanism of the localized tip of soft everting robot

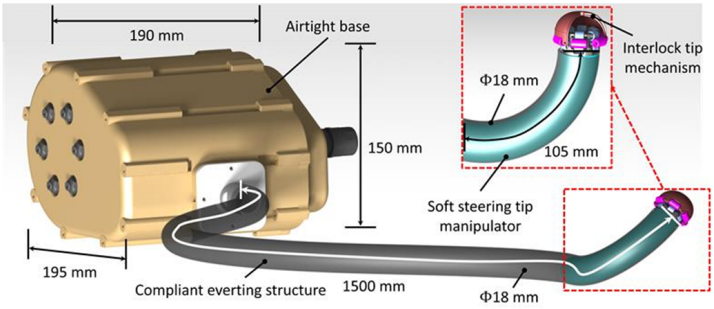

Figure 2: Localized tip of soft everting robot [2]

1.2 Aim and Objectives

This project aims to provide a tool to guide the design of a steering tip for soft everting robots. In order to accomplish this aim, this study investigates the relationship between the steering performance and design parameters, including manipulator dimensions, manipulator strength, and fabric properties, through both finite element analysis and experimental characterization.

1.3 Structure of Report

This study first gives a brief literature review in Section 2 on the steering actuation methods of soft everting robots, which includes the implementation of tendons, pouch motors, artificial muscles and steerable tips. The study also reviews the modelling approaches adopted to represent the physical properties of soft everting robots, which can be mainly classified as analytical or computational approaches. Subsequently, in Section 3, a finite element model is created and validated, which is used to investigate the relationship between the steering performance and design parameters. Additional, in Section 4, the study describes experimental characterization made, which focuses on design parameters that cannot be investigated by finite element analysis due to its limitation. A discussion about the achieved results is presented in Section 5 and finally the conclusion is summarized in Section 6.

2 Literature Review

2.1 Steering Mechanism

Steering is a vital function of soft everting robots. Soft actuators embedded in these robots provide greater adaptability and manoeuvrability than regular rigid robots, allowing them to operate in constrained and narrow environments. Over the past decade, the development of vine robots has provided valuable insights into various applications, including coral reef exploration [3], pipe inspection [4], and medical instrumentation [5]. The steering of soft everting robots is achieved by different types of actuators, including tendons, pouch motors, and artificial muscles.

2.1.1 Tendon

Tendon-based actuators are flexible and high-tensile strength cables, which are embedded along the length of the soft robot from base to top [6], shown in Figure 3. These tendons are actuated by base-mounted motors. During operation, the motor pulls the tendon, and the tension causes the body of the soft everting robot to bend towards a fixed direction, which is along the surface with the pulled tendon.

Tendon actuation allows the creation of repeatable, precise, and reversible shape change [7]. Local deformation is limited to only the prescribed path designed when the tendon is intergrated into the soft robot. The fact that tendons are flexible provides high compatibility with the soft structures. Less energy and control are required for such actuation, as there is only simple angle deflection in such a scenario. However, tendon-driven actuators have a lower efficiency of force transmission, with inevitable friction of the cable, derailment of the tendon, and inaccurate routing of the cable [8]. In addition, choosing tendon-driven actuators imposes significant manufacturing complexity, considering the possible need for complicated geometries.

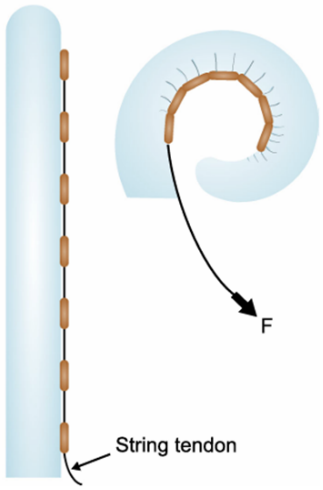

Figure 3: Tendon-driven actuator [7]

2.1.2 Pouch Motor

Pouch motors are considered a type of pneumatic actuator made of sealed, flexible pouches, as shown in Figure 4. During the pressurisation, the pouches are inflated and shortened. Under asymmetric inflation of different pouches, the pouch motor sets exhibit different changes in length at different locations, causing the soft robot to bend in a certain direction. Multiple pouch motor sets are used together to provide better steering with higher flexibility [9].

The biggest advantage of such an actuator is its light weight, as pouches contribute minimally to the overall structural weight. They can be simply manufactured by partially heat-sealing a tube of airtight, flexible material [9]. On the other hand, pouch motors have poor durability, which makes them susceptible to high-cycle loading. Pouch motors also have high nonlinearity, which adds more difficulty to accurately control them.

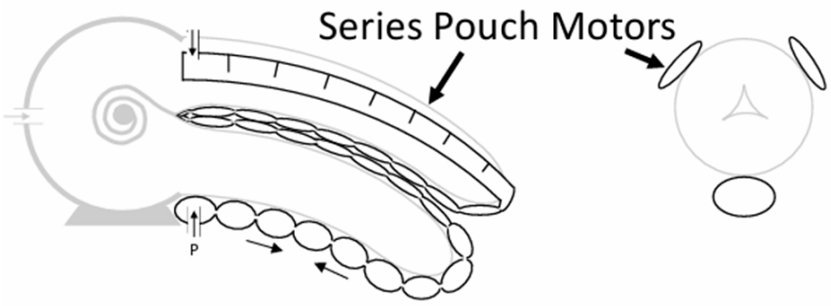

Figure 4: Tendon-driven actuator [9]

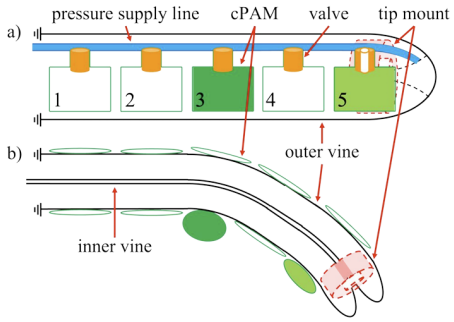

Figure 5: Cylindrical pneumatic artificial muscle [11]

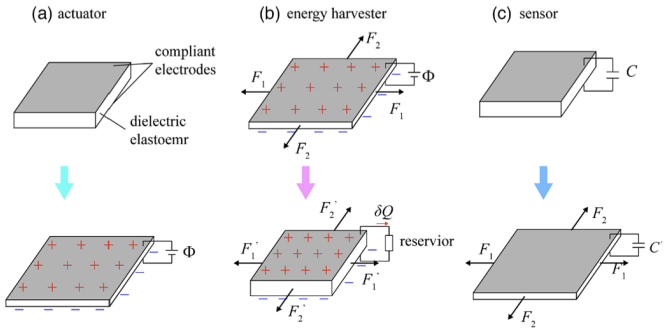

Figure 6: Dielectric elastomer actuators [12]

2.1.3 Artificial Muscle

Artificial muscle is a generic term for a class of materials and devices that can reversibly contract, expand, or rotate within one component due to an external stimulus [10]. Artificial muscles come in various forms, which include pneumatic artificial muscle (PAM) (Figure 5), dielectric elastomer actuators (DEA) (Figure 6), and many others.

Overall, artificial muscle is a lightweight and flexible actuator. The biggest advantage is its biomimetic property, making it most suitable for embedded actuation. However, such designs impose high complexity in manufacturing and control, and require specific power input depending on the type.

2.1.4 Steerable Tip

A steerable tip refers to a localized actuation system at the growing tip of the soft everting robot. The localized tip acts as the manipulator to control the steering of the entire vine robot. The actuation of the steering tip is performed in multiple different ways, including cable-driven (Figure 7), magnetic-driven (Figure 8), and so on.

Such actuation method is highly compact and modular, which provides a precise localized control. It is also an energy-efficient steering actuator, considering that actuation is required for only a localized region. However, as only the tip experiences steering, the steering range is highly restricted. Controlling multiple chambers at the same time also imposes a high level of control difficulty on such design.

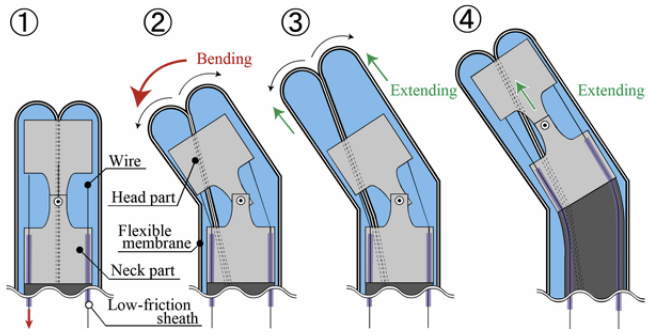

Figure 7: Cable-driven steerable tip [13]

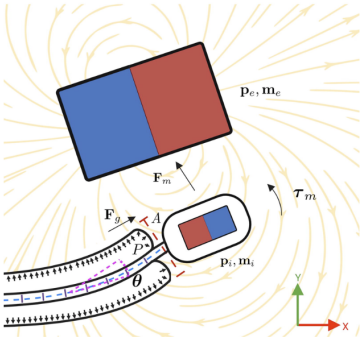

Figure 8: Magnetic-driven steerable tip [14]

Table 1: Comparison between different actuations used for steering

Actuator	Simplicity	Precision	Force Output	Limitations
Tendons	Low	High	High	High friction Complex routing
Pouch Motor	High	Moderate	Moderate	Low durability
Artificial Muscle	Low	Moderate	Depend on types	Power requirement
Steerable Tip	Moderate	High	Moderate	Short range

2.1.5 Comparison

The four types of steering actuators used in soft everting robots are compared in Table 1. Overall, tendons provide a high force output, pouch motors have the simplest design with high manufacturability, artificial muscles are biomimetic, and steerable tips offer high precision in localised area.

2.2 Modelling of Soft Everting Robot

Considering the fact that soft everting robots consist of nonlinear materials, complex and variable geometries, and complex interaction forces, modelling them is considered as a huge challenge. Multiple approaches have been developed to model the soft robot, which can be mainly classified as analytical modelling and computational modelling.

2.2.1 Analytical Model

Several analytical models are developed to capture and describe the physical property of the soft everting robots. Mainly through three approaches: kinematics, quasi-Statics, and dynamics.

Kinematics models, accompanied by the force-balanced models, are employed to predict the robot shapes based on the geometry relationships. The model initially originates from the constant curvature assumption, which simplifies the complex deformation of the robot into manageable geometric parameters. The model further continues to incorporate concepts of actuator stiffness, body deformation and variable length due to growth [1]. Such model is one of the simplest models, making it computationally efficient, and easy to implement. However, such model has a relatively low accuracy, as it ignores many important factors, some of which are discussed in the other models [15].

Quasi-static models refer to the analysis that is capable of neglecting dynamics factors. This assumption is valid when the movement of the object is slow enough to be considered as in an equilibrium state, with balanced inertial forces and thus negligible dynamics. The model originates from equilibrium internal pressures, and further on takes eversion losses, external forces and buckling and bending loads into consideration [1]. Such model provides moderate simplicity, but is still able to have an adequate accuracy as it accounts for material effects and force-pressure balance. However, quasi-static model is extremely restricted to slow motions only, which cannot be applied to rapidly changing environments or fast movements.

Dynamic models integrate the time-dependent physical behaviours that are neglected in the previous models, which includes consideration on the inertial effects, damping effects. This model is not limited to slow motions only, and is also suitable for fast movements. This model is the most accurate analytical model as it captures time-dependent behaviours, and it has a higher fidelity. In exchange, dynamic models require relatively higher computational cost, which is more-time consuming [16]. This model also cannot analyse complicated problems like complex geometry or multi-physics.

2.2.2 Computational Model

Finite element analysis (FEA) is the most common form of computational models. It is a numerical method used for solving complex physical problems by breaking down structures into smaller, manageable elements [17]. This analysis method is able to capture nonlinearity, and also supports complicated geometries. In soft robotics, finite element analysis is able to capture

Table 2: Comparison between different models of soft everting robots

Model	Computational Efficiency	Accuracy	Suitable Scenario
Kinematics	High	Low	Geometry prediction
Quasi-statics	Moderate	High for slow motions	Slow Motion
Dynamics	Low	High	Fast Motion
FEA	Lowest	Highest	Large deformation Nonlinear property

internal forces, strains, and stresses, and can predict both buckling and anisotropy, providing more realistic results than analytical modelling methods[18]. However, FEA requires a high computational cost with the need for 3D dynamic simulations. The need for material characterization and mesh refinement is complex and time-consuming as well.

2.2.3 Comparison

The modelling approaches used in soft everting robots are compared in Table 2. For analytical models, kinematic models offer the highest computational efficiency, quasi-static models have a high accuracy for slow motions, and dynamic models achieve a high accuracy even for fast motions. As a computational model, finite element analysis provides a higher level of accuracy, but is computationally intensive.

2.3 Conclusion

In summary, the study reviews a variety of steering actuators and modelling approaches developed for soft everting robots. For steering actuators, tendons, pouch motors, artificial muscles, and steerable tips offer different trade-offs in terms of force output, manufacturability, precision, and control complexity, as shown in Table 1. For the modelling approaches, kinematics, quasi-statics, dynamics and finite element analysis capture the physical properties of soft everting robots with varying levels of computational efficiency and accuracy, as shown in Table 2.

3 Finite Element Analysis of the Steering Mechanism

Soft everting robots consist of complex geometries, large deformation, and also highly nonlinear material, which makes finite element analysis a suitable analysis approach for investigating the physical behaviours, like the steering performance. For design parameters like manipulator dimension, manipulator material, or fabric strength, it typically requires material and time cost for new soft everting robots for experimental characterization. By using FEA instead, the lengthy iterative experimentation can be avoided [18].

3.1 Modelling Approach

In order to conduct an investigation into certain design parameters, a prototype is first developed, which acts as a standard reference for further comparison. The finite-element models consist of two main parts: the fabric and the steering manipulator, which are modelled separately and assembled together thereafter.

The software used for FEA is Abaqus, which is well-suited for modelling nonlinear material properties with predefined hyperelastic material models. The solver used is the dynamic explicit solver, which is more suitable for material nonlinearities. It is also a relatively efficient solver for short-duration events, and there is no need for convergence iterations. An overall simulation time of 1 second is applied for this model.

3.1.1 Modelling of the Fabric

The typical fabric used in soft everting robot is ripstop nylon, which has embedded reinforcement grid patterns within. The prototype fabric has a thickness of 0.05 mm and a grid length of 4 mm. The fabric sample diameter is set to 18 mm. The developed model is shown in Figure 9. The length of the fabric is set as 208 mm, which is sufficient to cover the whole manipulator and at the same time provides a complete reinforcement grid at both ends.

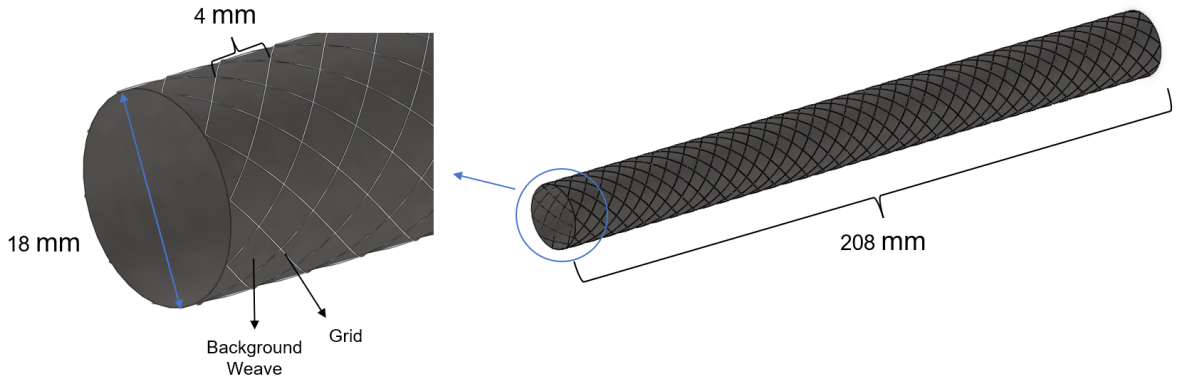

Figure 9: Finite element model of fabric

Ripstop nylon fabric is a non-homogeneous material consisting of a reinforcement grid embedded in a base fabric of standard nylon weave. These two components contain material of different deniers, which is a unit of measure for the linear mass density of fibres [19]. The grid pattern can be considered as homogeneous nylon, while the background weave is considered a composite material. In this study, only the elastic behaviour of the material influences the results, and therefore both sections are defined individually as shown in Table 3.

Growth pressure is applied to the inner surface of the fabric. This study aims to investigate the problem in quasi-static conditions, therefore smootstep is applied to the growth pressure increment, providing a smooth transition of a variable between two desired magnitudes. The smoothstep is computed as presented in Equation 1.

$$\text{Smoothstep}(x, a, b) = 3t^2 - 2t^3, \quad t = \frac{x-a}{b-a} \tag{1}$$

where x is the input variable to be interpolated, which is considered the growth pressure in this case. a and b refer to the initial and final values of x, and t is the normalized value of x in the range of [a,b], scaled to [t_1,t_2]. At t_1=0s, the magnitude of the growth pressure is 0, and at t_2=0.5s, the magnitude of the growth pressure reaches its maximum, which is kept at 15 kPa for further comparison.

Table 3: Elastic behaviour of different sections of the fabric [20] [21]

Material Section	Young's Modulus (MPa)	Poisson's Ratio
Reinforcement Grid	3000	0.3
Background Weave	30	0.3

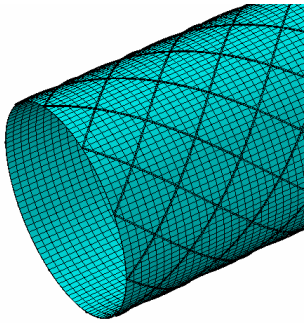

Figure 10: Illustration of the mesh refinement of fabric model

The mesh refinement of the fabric model is shown in Figure 10. The whole component is meshed using explicit C3D8R elements, which are 8-node linear bricks with reduced integration and hourglass control. The grid section and the background weave section have different global seeding sizes, set to 0.2 and 0.5, respectively. The overall number of elements in the fabric is 155316.

3.1.2 Modelling of the Steering Manipulator

The finite element model of the steering manipulator is shown in Figure 11, with its relevant dimensions illustrated in Figure 12. The manipulator mainly consists of two nonlinear materials, which are set as Dragonskin 20 and Ecoflex 20 for this prototype. These two materials are free to move according to each other, with no friction force between them. Two plates are tied to the two ends of the manipulator, which help to seal the pressure inside the manipulator. These plates are set as rigid bodies, with their reference point at the centre, preventing any deformation of the plate in the simulation.

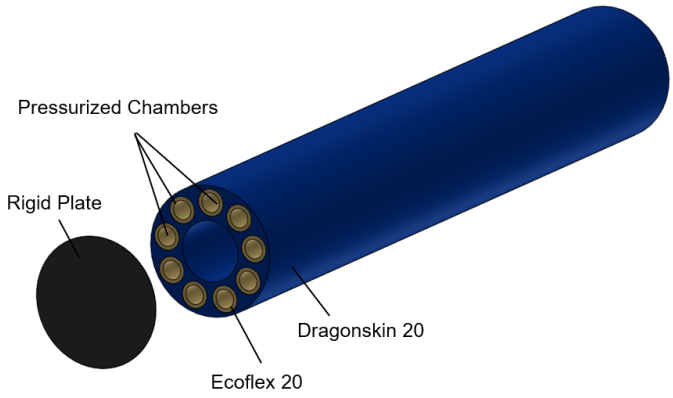

Figure 11: Finite element model of steering manipulator

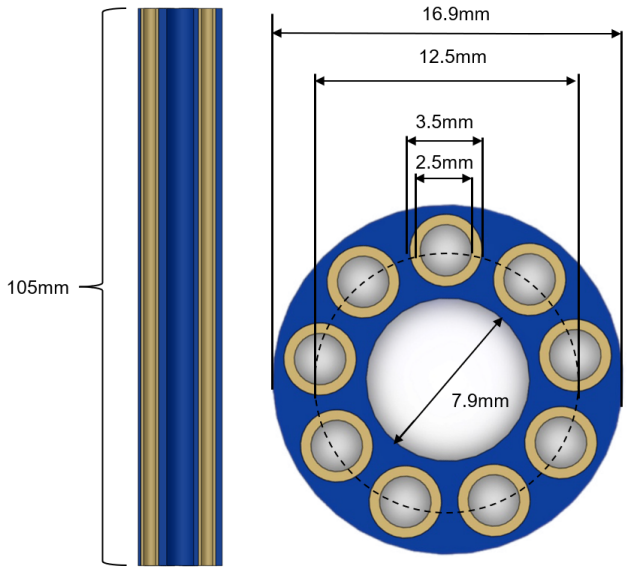

Figure 12: Section view of manipulator model with dimensions

Dragonskin 20 and Ecoflex 20 have high nonlinearity. Their elastic behaviour cannot be represented by only the Young's modulus and Poisson's ratio. Considering the available nonlinear model in Abaqus, these materials are defined by using the third-order Yeoh model. This model fits the stress-strain behaviour of a material according to the Equation 2 [22]. Three coefficients C_1, C_2, and C_3 are required to define a nonlinear material. By using such a method, Dragonskin 20 and Ecoflex 20 are defined as shown in Table 4.

$$\sigma_{\text{uniax}} = 2\left(\lambda^2 - \frac{1}{\lambda}\right)\sum_{i=1}^{3} i \cdot C_i (I_1 - 3)^{i-1} \tag{2}$$

Steering pressure is applied to the fixed three chambers, exerting force on the rigid plate, as shown in Figure 13. The rigid plate is divided into several parts, shown in Figure 14, so that a difference in steering pressure of each section causes an imbalance on the plate, thus bending the manipulator. Smooth step interpolation is also applied to the steering pressure. At t_1=0s, the magnitude of the steering pressure is 0, and at t_2=1s, the magnitude of the steering pressure reaches the maximum, which is kept as 300 kPa for further comparison.

Table 4: Yeoh model coefficients of Dragonskin 20 and Ecoflex 20 [23]

Material	C_1	C_2	C_3
Dragonskin 20	0.1062	0.0018	0
Ecoflex 20	0.0077	0.0002	0

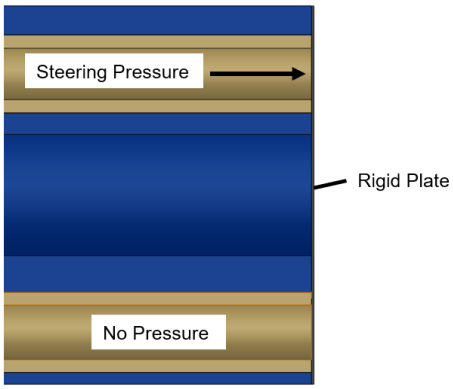

Figure 13: Illustration of the steering pressure in the manipulator

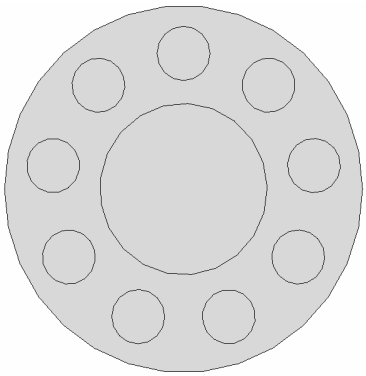

Figure 14: Sectioned rigid plate

The mesh refinement of the manipulator is conducted with the same C3D8R element from the explicit library as before. The meshing of each component is carried out separately. The meshing of the Dragonskin 20 component, shown in Figure 15, has an approximate global size of 0.3, as it has a complex geometry that needs more elements to define. Local seeding is applied to the length of the component, with the number of elements controlled to be 50. The Ecoflex 20 component, shown in Figure 16, has a global size of 0.5. To mesh the component according to its cylindrical geometry, local seeding defines 2 elements along the radial direction, 36 elements along the tangential direction, and 50 elements along the longitudinal direction. Rigid plate is not a crucial component, therefore, it has an approximate global size of 0.6, shown in Figure 17. The overall meshing of the manipulator is presented in Figure 18, with a total element count of 130872.

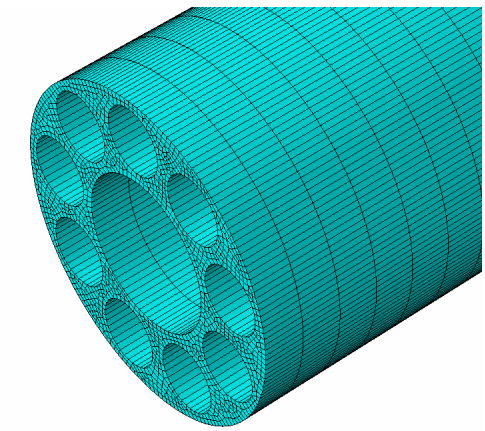

Figure 15: Illustration of the mesh refinement of Dragonskin 20

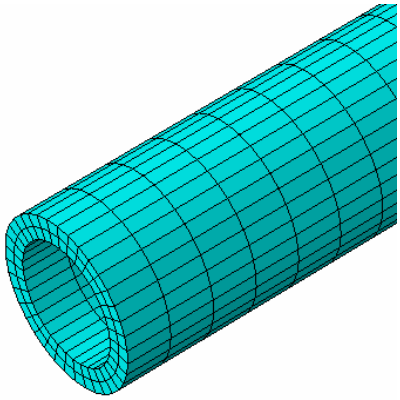

Figure 16: Illustration of the mesh refinement of Ecoflex 20

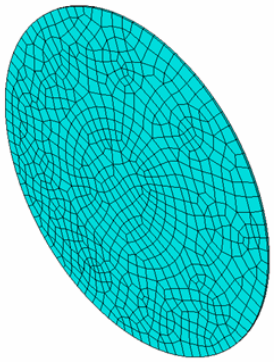

Figure 17: Illustration of the mesh refinement of rigid plate

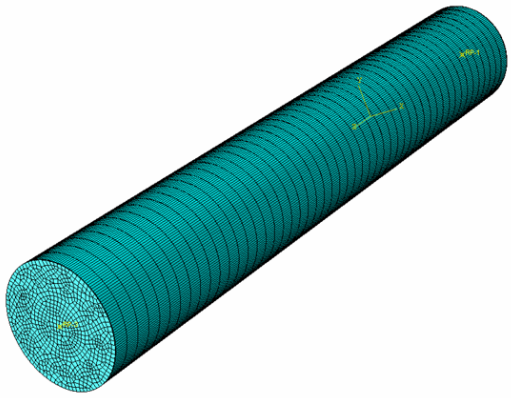

Figure 18: Illustration of the mesh refinement of steering manipulator

3.1.3 Assembly Setting

The finite element models of the fabric and the steering manipulator are assembled by adding the manipulator to the centre of the fabric. General contact is defined globally throughout the model. The global property of such is set, with its tangential behaviour being frictionless, and the normal behaviour having 'Hard' contact pressure-overclosure, default constraint enforcement method, and allowing separation after contact.

3.2 Result

3.2.1 Steering angle of the prototype

Under the conditions set in the previous section, with a steering pressure of 300 kPa, the steering performance of the soft everting robot is shown in Figure 19. The result exhibits a constant curvature along the length of the manipulator.

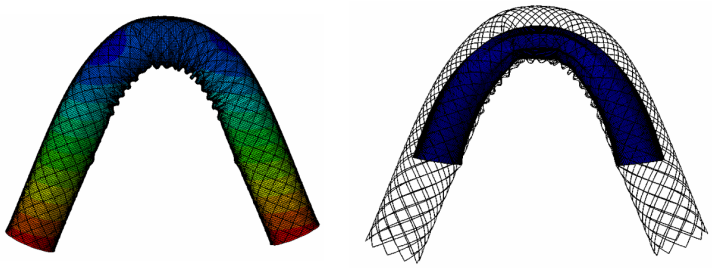

Figure 19: Steering performance of the prototype with 300 kPa steering pressure and 15 kPa growth pressure

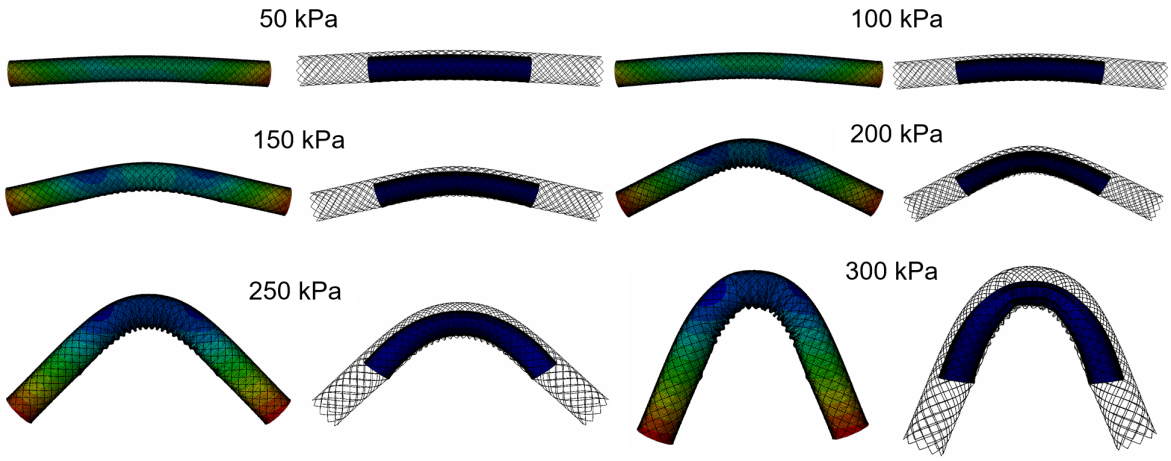

Figure 20: Steering performance of the prototype with varying steering pressure at 15 kPa growth pressure

The developed model of the soft everting robot needs to be validated before it can be used for further comparison. As the model simulates a quasi-static problem, the steering performance at the final steering pressure is expected to show higher accuracy. The maximum steering pressure of the prototype is varied from 50 kPa to 300 kPa in steps of 50 kPa, and the steering performance is shown in Figure 20.

The steering capability is quantified by the steering angle of the soft everting robot at a specific steering pressure input. A larger steering angle value indicates that a lower pressure input is required to reach a desired steering angle, thus exhibiting a better steering performance.

To deduce the steering angle of the simulations, three coordinates are randomly selected at each end of the fabric, with six coordinates selected in total, represented as points A_1, A_2, and A_3 for the first surface, and B_1, B_2, and B_3 as the second surface. Three points are sufficient to define a surface, with respect to its normal vectors:

$$\vec{n}_A = (\vec{A}_2 - \vec{A}_1) \times (\vec{A}_3 - \vec{A}_1) \tag{3}$$

$$\vec{n}_B = (\vec{B}_2 - \vec{B}_1) \times (\vec{B}_3 - \vec{B}_1) \tag{4}$$

The angle θ between the normal vectors is taken as the steering angle:

$$\theta = \cos^{-1}\left(\frac{\vec{n}_A \cdot \vec{n}_B}{\|\vec{n}_A\| \cdot \|\vec{n}_B\|}\right) \tag{5}$$

Table 5: Steering angle under varying steering pressure of the prototype under 15 kPa growth pressure

Steering Pressure (kPa)	0	50	100	150	200	250	300
Steering Angle (Degrees)	0	4	11	34	52	88	134

The steering angles under different steering pressure are presented in Table 5.

3.2.2 Manipulator Length and Steering Angle

Manipulator length is a design parameter that is related to the steering angle. It is time-consuming to prepare different manipulators of different lengths, therefore, this is investigated through finite element analysis. The length of the manipulator from the prototype is 105 mm, and this is now varied between 75 mm to 135 mm with a step of 15 mm.

The steering performance and the related steering angles are shown in Figure 21 and Figure 22. As the manipulator decreases from 105 mm to 75 mm, the steering angle decreases from 134 degrees to 90 degrees. It is also shown that short manipulators are more difficult to retain a constant curvature pattern than the longer ones. As the manipulator increases from 105 mm to 135 mm, there is an slight increase in the steering angle from 134 degrees to 148 degrees. A longer manipulator is able to retain the uniform curvature pattern along the length, but it can be seen that a longer steering distance is required to steer a longer manipulator, with the radius of steering changing from 22 mm to 42 mm.

3.2.3 Manipulator Material and Steering Angle

The material used for the main body of the manipulator is not limited to Dragonskin 20. Multiple other nonlinear material options are shown in Table 6, defined according to the third-order Yeoh model.

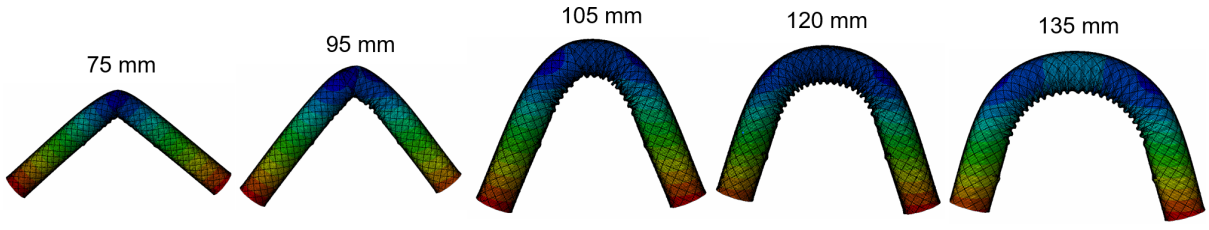

Figure 21: Steering performance of the soft everting robot with varying manipulator length at 15 kPa growth pressure

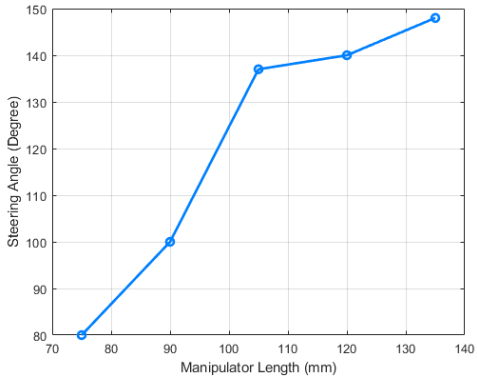

Figure 22: Steering angle of the soft everting robot with varying manipulator length at 15 kPa growth pressure

Table 6: Yeoh model coefficients of Ecoflex 50, Dragonskin 10, Dragonskin 20 and Dragonskin 30 [23]

Material	C_1	C_2	C_3
Ecoflex 50	0.011771	0.000159	0
Dragonskin 10	0.039695	0.000627	0
Dragonskin 20	0.1062	0.0018	0
Dragonskin 30	0.1313	0.002546	0

The steering performance with different manipulator materials is shown in Figure 23. It can be seen that for samples using Ecoflex 50 and Dragonskin 10, the manipulator cannot bend the fabric at a high steering pressure, and as for the sample using Dragonskin 30 instead of Dragonskin 20, the result retains a constant curvature pattern, but shows a reduction in the steering angle from 134 degrees to 87 degrees.

3.2.4 Fabric Strength and Steering Angle

Fabric is another aspect that influences the steering performance of the soft everting robots. In finite element analysis, different fabric materials are represented by variations in the fabric strength. In this section, the Young's modulus of the background weave of the fabric changes

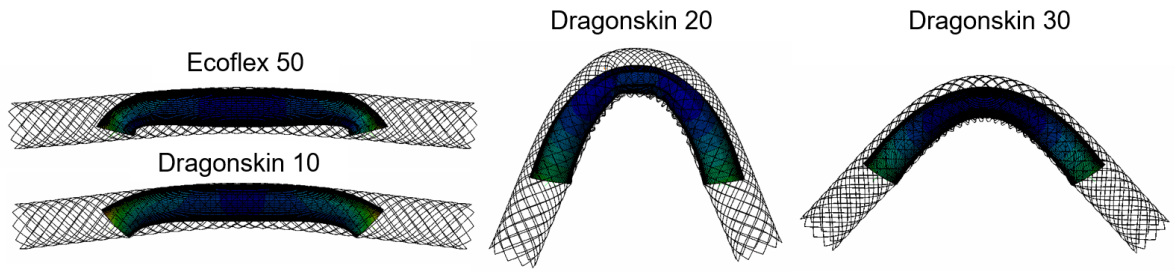

Figure 23: Steering performance of the soft everting robot with different manipulator material at 15 kPa growth pressure

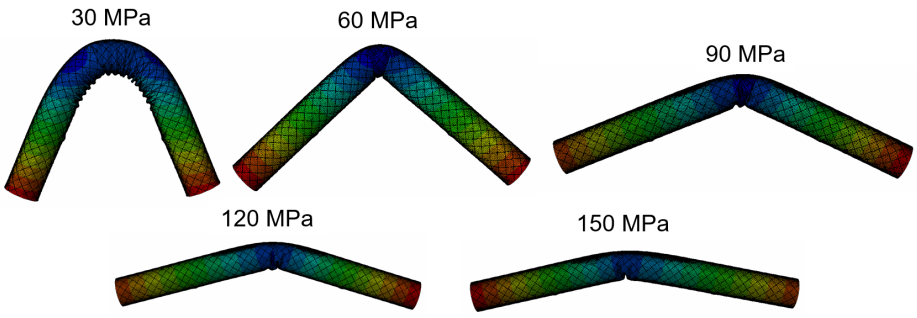

Figure 24: Steering performance of the soft everting robot with varying fabric strength at 15 kPa growth pressure

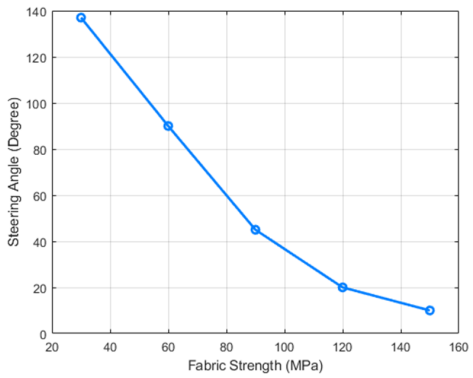

Figure 25: Steering angle of the soft everting robot with varying fabric strength at 15 kPa growth pressure

from 30 MPa to 150 MPa in steps of 30 MPa, to investigate its influence to the steering performance. It should be noted that a fabric with lower strength cannot withstand the required growth pressure and may cause excessive distortion.

The steering performance and the related steering angles are shown in Figure 24 and Figure 25. The result shows that lower fabric strength leads to a relatively higher steering angle, as the angle decreases from 134 degrees to 5 degrees when the fabric strength increases from 30 MPa to 150 MPa. In addition, the geometry of the soft everting robot no longer exhibits a constant curvature, which is not considered ideal steering performance.

However, in reality, different fabric selections cannot be solely represented by material strength. As anisotropic material, fabrics have complex mechanical properties such as elasticity, flexibility, and ductility, which directly influence how the robots deform. These design parameters are investigated by through experimental characterisation in Section 4.

4 Experimental Characterisation of Everting Materials

4.1 Description of Everting Materials

The selection of fabric plays a critical role in determining the steering performance of soft robots. Due to limitations in the finite element analysis approach, experimental characterisation is conducted to investigate how choices of fabrics influence the steering capability.

Ripstop nylon is commonly used in soft everting robots, with reinforced cross-hatch grid patterns providing high tear resistance and durability. For this study, five commercially available ripstop nylon fabrics with thicknesses appropriate for soft robotic applications were selected for experimental characterization, as illustrated in Figure 26. Additionally, plastic, as a common selection for other soft robots [24], is also included for comparative analysis. The relevant parameters of these materials, including their thickness and length of the grid patterns, are presented in Table 7.

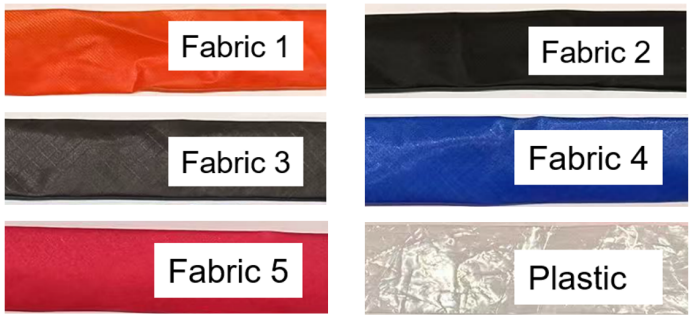

Figure 26: Illustration of fabric materials

Table 7: Parameters of six everting materials

Fabric Number	Thickness (mm)	Grid Length (mm)
Fabric 1	0.03	1
Fabric 2	0.05	1
Fabric 3	0.05	4
Fabric 4	0.06	3
Fabric 5	0.09	3
Plastic	0.05	/

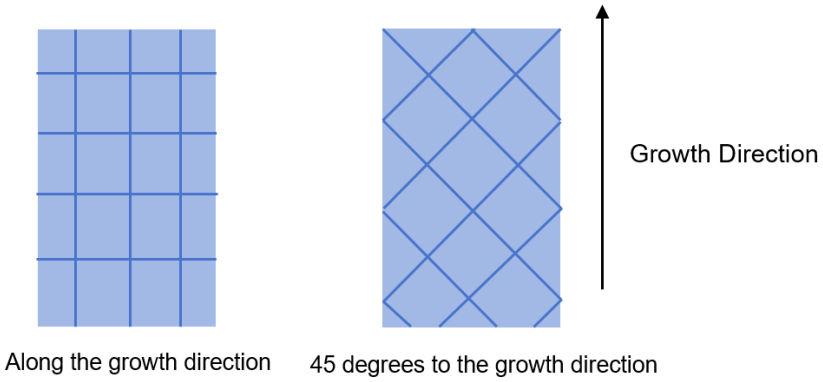

Figure 27: Grid Configurations

Based on the characterized material parameters, the selected materials were fabricated into cylindrical samples suitable for soft robotics applications. These samples were prepared in various configurations, which were subsequently compared to evaluate their performance. Four different samples are prepared for each material, featuring diameters of either 18 mm or 25 mm. The orientation of the reinforcement grid also varies during preparation, with configurations aligned either along the growth direction or at a 45-degree angle to it (Figure 27) .

4.2 Characterisation of Steering Angle

4.2.1 Experimental Setup

The steering performance of soft robots with different fabric selections is tested by using the soft everting robot setup as shown in Figure 28, with its corresponding flow chart shown as Figure 30. The tested fabric sample is assembled onto the everting structure, which is then connected to the airtight base. A string is suspended from the tip of the robot to prevent it from touching the ground, thus minimizing the effect of friction.

The power of the setup is provided by an AC-DC electric converter [RS 765-4676]. The growth pressure and the steering pressure are regulated, as the PC console sends a command to the microcontroller [Teensy 4.1], which outputs a PWM signal, regulating the duty cycle of the electric input of the solenoid valves [ITV2010, G3/8, SMC)] and consequently the pressure input of the soft everting robot.These are incorporated in the control box, shown in Figure 29.

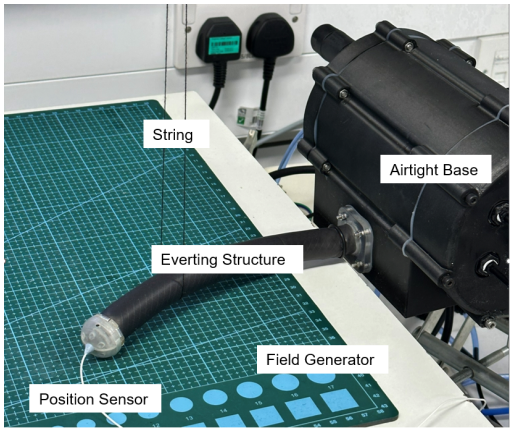

Figure 28: Experiment setup for testing steering angle

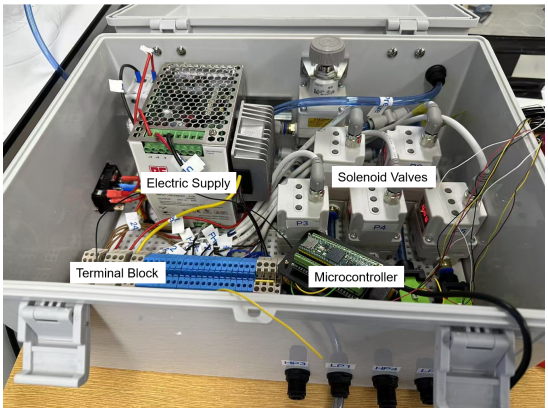

Figure 29: Control Box for testing steering angle

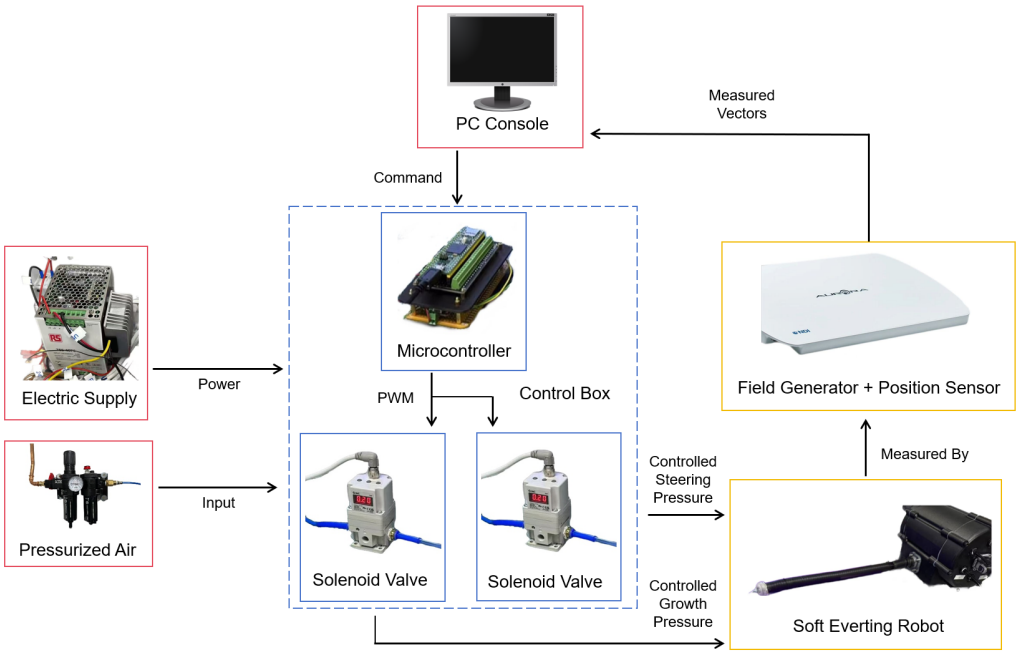

Figure 30: Flow chart for testing steering angle [25]

The steering angle is measured by adding a position sensor at the steerable tip. A position sensor is attached at the end of the fabric, and accompanied by an electromagnetic field generator [Aurora, NDI] underneath, the position vector of the sensor is measured and recorded. The change in angle of the position vectors before and after the steering can be calculated using Equation 5, which is equivalent to the steering angle.

4.2.2 Experimental Protocol

The tested sample is assembled with the soft everting robot. The initial position vector of the sensor is recorded. Pressurised air and electric power are supplied into the setup. The input

growth pressure and the steering pressure are regulated by sending commands from the PC console. The growth pressure is fixed at a certain level between 0-20 kPa, while the steering pressure is linearly increased from 0 kPa to 300 kPa over 20 s. Three fixed chambers of the soft manipulator are being pressurized while the others are kept unpressurised to keep the steering direction the same for all trials.

Three trials are conducted for the same condition. Subsequently, the experiment is repeated with six different fabric materials, two different sample diameters, and four different growth pressures (5 kPa, 10 kPa, 15 kPa, and 20 kPa), as well as two reinforcement grid configurations, aligned either at 0-degrees or 45-degrees to the growth direction.

4.2.3 Results for the Steering Angle

The change of steering angle with steering pressure under different growth pressure, with a grid configuration at a 45-degree angle to the growth direction and a diameter of 18 mm, is shown in Figure 31. Generally, the steering angle increases as the steering pressure increases.

At low growth pressure of 0 kPa, the steering angles of Fabric 2, Fabric 3, and Fabric 4 exhibit similar steering angle, reaching approximately 175 degrees at a steering pressure of 300 kPa. Fabric 1 shows a higher angle at 190 degrees, while Fabric 5 shows a lower angle at 140 degrees. Relating to the material parameters, shown in Table 7, this is an indication that at low growth pressure, a thicker fabric results in a larger steering angle.

As the growth pressure increases, the steering angle of every sample starts to decrease, which means it is more difficult for the soft everting robot to steer at a higher growth pressure. At an intermediate growth pressure of 10 kPa, among the ripstop nylon materials, Fabric 1 undergoes the largest decrease in steering angle from 190 degrees to 130 degrees. Fabric 3 also undergoes a large reduction from 175 degrees to 120 degrees. By contrast, Fabric 2 and 3 have a smaller reduction from 175 degrees to 135 degrees. This causes a minor difference between Fabric 1 and Fabric 2 and 3. Fabric 5 has the smallest reduction in angle, from 140 degrees to 120 degrees.

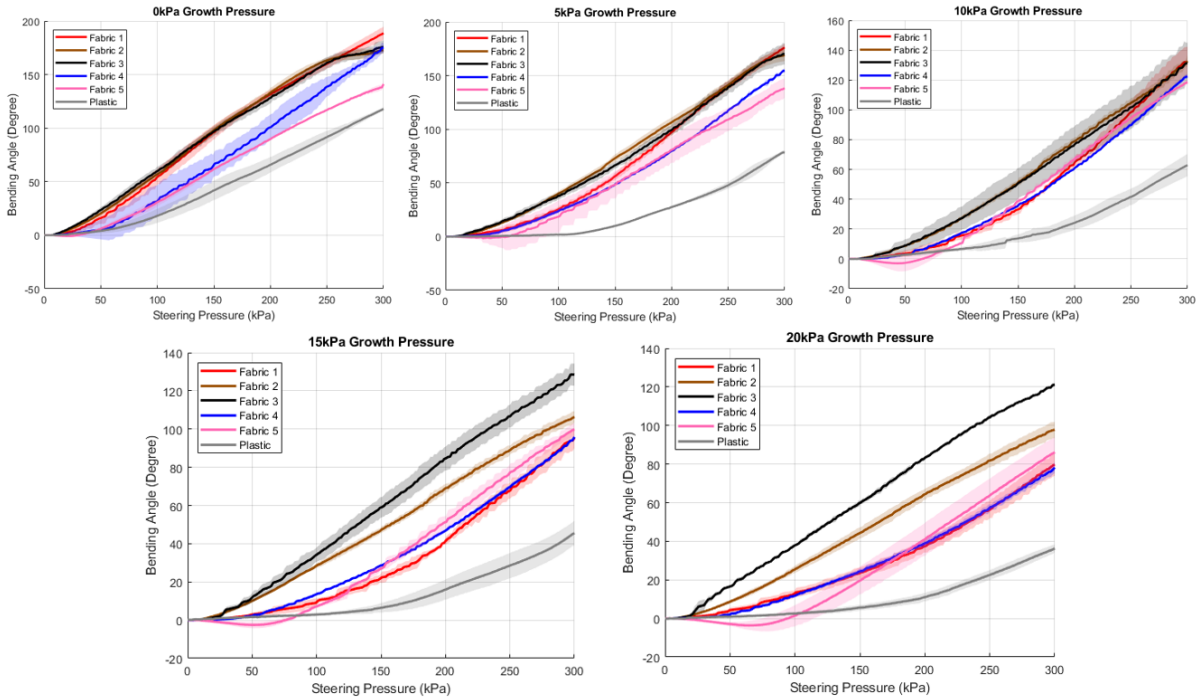

Figure 31: Change in steering angle with steering pressure under varying growth pressures, with a grid configuration at a 45-degree angle to the growth direction and a diameter of 18 mm

At high growth pressure of 20 kPa, Fabric 3 achieves the largest steering angle, reaching 120 degrees at 300 kPa steering pressure. This is followed by Fabric 2, Fabric 5, Fabric 1, and Fabric 4, with final steering angles of 95 degrees, 82 degrees, 80 degrees, and 79 degrees, respectively. This result is investigated in Section 4.3

As for the homogenous plastic material, it shows an indistinct difference with the ripstop nylon materials at 0 kPa growth pressure, with a final steering angle at 120 degrees. As the plastic fabric is pressurized, the steering angle dramatically decreases to 80 degrees at 5 kPa growth pressure, and continues to decrease to only 38 degrees at 20 kPa growth pressure. This has a significant difference from the others, indicating that the steering performance of plastic is substantially poorer than ripstop nylon fabric when the reinforcement grid is oriented at 45 degrees to the growth direction.

The result of the steering angle with the same grid configuration but with a larger diameter of 25 mm is similar to the previous result, as shown in Figure 32. At low growth pressure of 0 kPa, most nylon fabrics have similar final steering angles at about 170 degrees. By contrast, the thickest sample, Fabric 5, exhibits a much smaller angle at about 135 degrees. As the growth

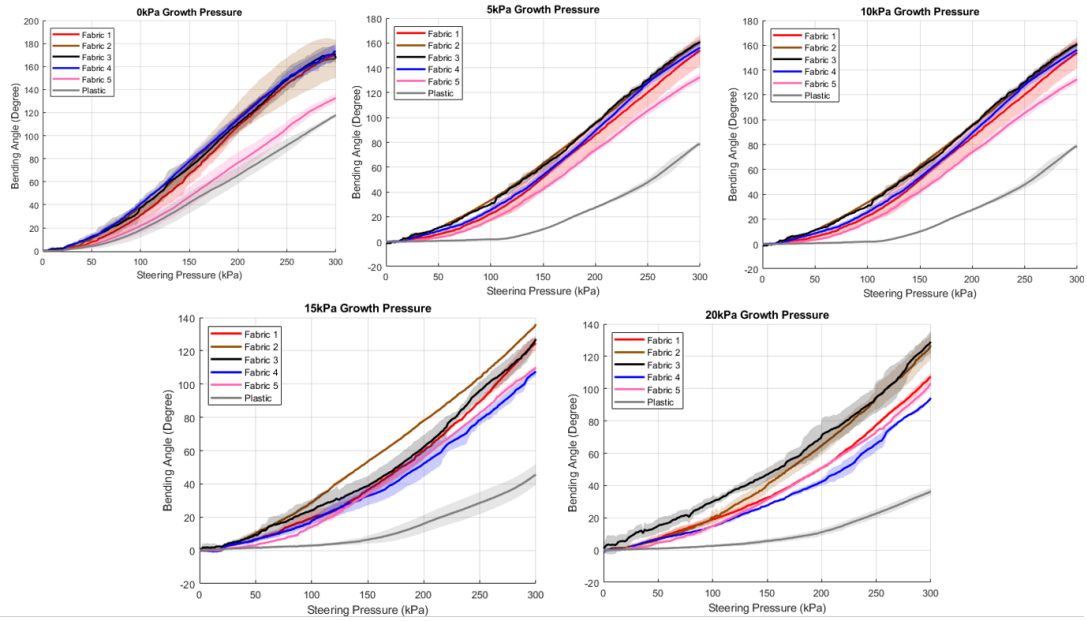

Figure 32: Change in steering angle with steering pressure under varying growth pressures, with a grid configuration at a 45-degree angle to the growth direction and a diameter of 25 mm

pressure increases, all fabrics exhibit a decrease in steering angle. At high growth pressure of 20 kPa, Fabric 3 has the highest final steering angle at 120 degrees, followed by Fabric 2 at 100 degrees, Fabric 5 at 82 degrees, Fabric 1 at 80 degrees, and Fabric 4 at 79 degrees. By contrast, the steering performance of the plastic fabric sample remains significantly different from the others under this condition.

The change of steering angle with steering pressure under different growth pressure, with a grid configuration of 0-degree angle to the growth direction and a diameter of 18 mm, is shown in Figure 33. At low growth pressure of 0 kPa, the steering angle result is similar to the 45-degree configuration samples. Thinner fabric, such as Fabric 1, exhibits a relatively larger angle at 170 degrees, while thicker fabric, such as Fabric 5, exhibits a smaller angle at only 104 degrees. This suggests that fabric thickness is the predominant factor in this situation.

As the growth pressure increases, the steering angle drops dramatically. At an intermediate growth pressure of 10 kPa, Fabric 1 and Fabric 2 drop from 170 degrees to 100 degrees, Fabric 3 drops from 140 degrees to 80 degrees, and Fabric 4 and 5 drop to only 40 degrees. This shows a huge contrast when compared with samples of different grid configurations.

This trend also applies to higher growth pressure conditions. At a growth pressure of 20 kPa,

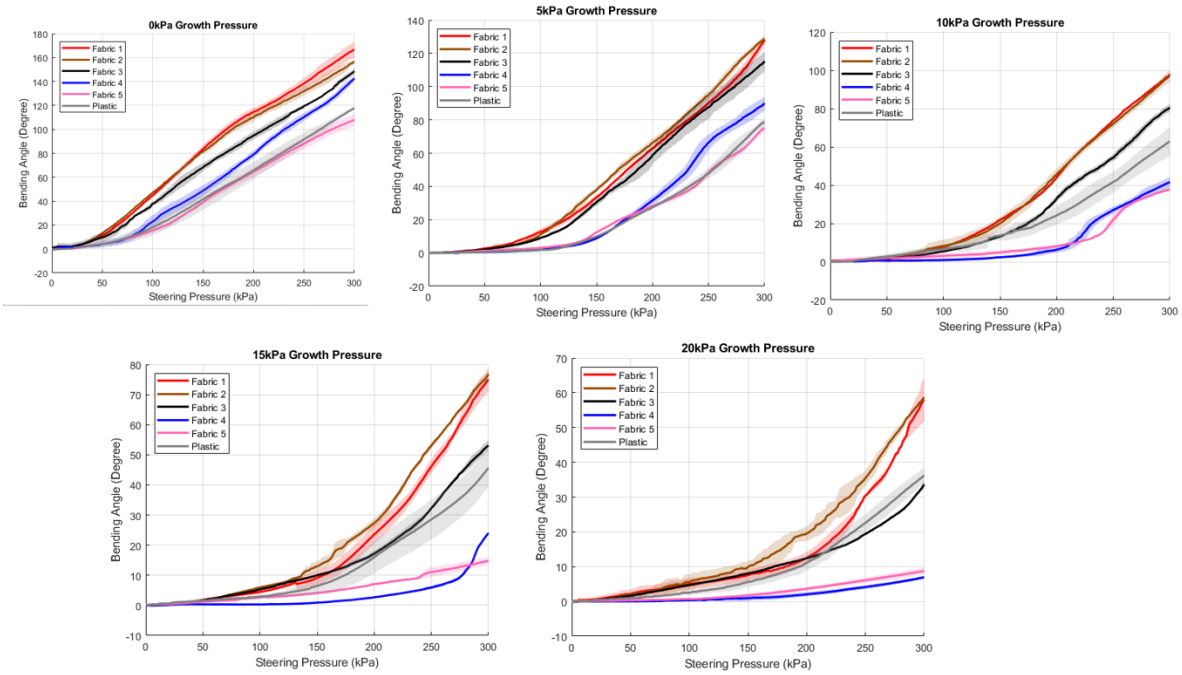

Figure 33: Change in steering angle with steering pressure under varying growth pressures, with a grid configuration at a 0-degree angle to the growth direction and a diameter of 18 mm

Figure 34: Buckling effect

Figure 35: Wrinkling effect

Fabric 1 and 2 drop from 100 degrees to 60 degrees, Fabric 3 drops from 80 degrees to 30 degrees, and Fabric 4 and 5 drop to 10 degrees. Such ranking of steering angle between different fabric is the same for every growth pressure, which means that thickness thickness remains the dominant factor for samples with a 0-degree grid configuration. At high growth pressure, it can be seen that the steering angle doesn't increase proportionally with the increase in steering pressure. At low steering pressure, there is barely any increase in the steering angle, but when the steering pressure reaches 200 kPa, the rate of change of angle increases sharply. This phenomenon results from buckling, where the manipulator cannot bend the fabric until buckling occurs, as shown in Figure 34. This is a unique behaviour that only appears with a 0-degree grid configuration at high growth pressure, whereas in other cases, wrinkling takes place instead, as shown in Figure 35.

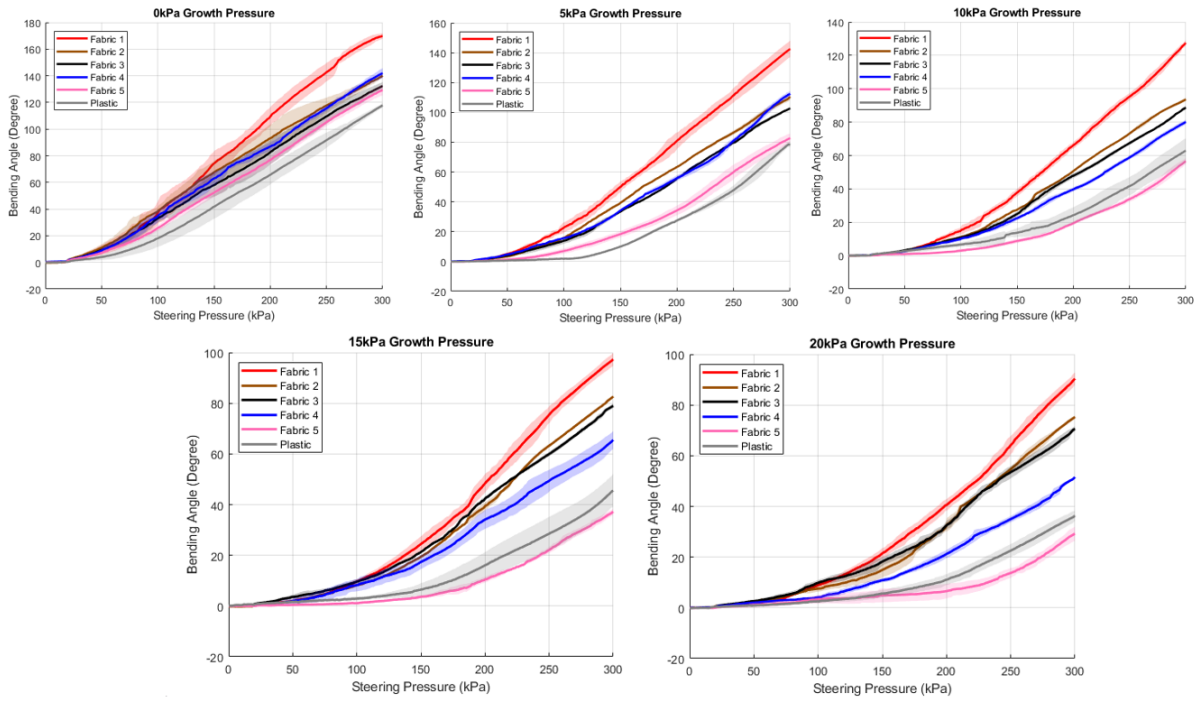

Figure 36: Change in steering angle with steering pressure under varying growth pressures, with a grid configuration at a 0-degree angle to the growth direction and a diameter of 25 mm

When comparing with homogenous plastic material, it is shown that there is no obvious difference between plastic and ripstop nylon fabrics, which means that the steering performance of the soft everting robots using plastic fabrics is more similar to the ones using 0-degree grid configuration nylon fabric.

The result of the steering angle with grid configuration of 0-degree angle to the growth direction and a diameter of 25 mm is similar to the previous result, as shown in Figure 36. At low growth pressure of 0 kPa, all fabrics show similar steering performance as the ones with 45-degree grid configurations. There is a linear relationship between the steering angle and the steering pressure. At higher growth pressures, the rate of change of steering angle with the steering pressure is non-constant, showing a sudden increase at approximately 200 kPa steering pressure. The steering angle drops dramatically with a rise in growth pressure. From 0 kPa to 20 kPa growth pressure, Fabric 1 has the largest relative steering angle, which has a reduction in steering angle from 170 degrees to 90 degrees. Fabric 5 has the smallest steering angle, which drops from 130 degrees to 28 degrees. Buckling can still be observed under such situation, as indicated by the non-lineal relationship between the angle and steering pressure.

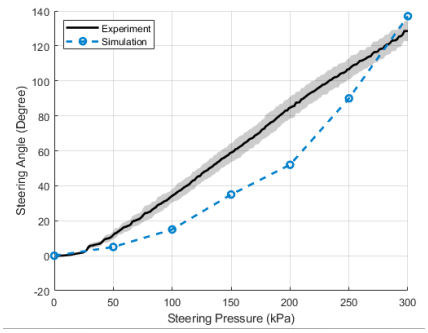

Figure 37: Comparison of steering angles between FEA and experimental results

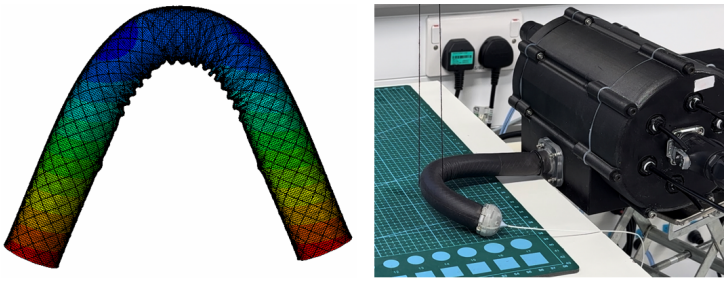

Figure 38: Steering performance of FEA and experimental results

4.2.4 Comparison between FEA and Experimental Results

In the experiment, the trial using Fabric 3 samples with 18 mm diameter and 45-degrees grid configuration under 15 kPa growth pressure is the same operating condition as the finite element analysis in Section 3.2.1. The steering angles under various steering pressure is shown in Figure 37, with the relevant steering performance of the results shown in Figure 38. It is shown that the experiment and simulation presents similar results, which validates the reliability of the experimental characterisation.

4.3 Contraction Ratio of Everting Materials

As discussed in Section 4.2.3, at high growth pressure, the steering performance samples with a grid configuration at a 45-degree angle to the growth direction cannot be explained by any given design parameters of the fabrics. A new feature of the fabric is investigated - the contraction ratio.

Fabric samples with grid configurations of a 45-degree angle to the growth direction exhibit a distinctive behaviour, as the cylindrical structure contracts along the growth direction when it is pressurized, as shown in Figure 39. In contrast, samples composed of homogeneous materials, such as plastic, exhibit extension rather than contraction under pressurization.For different fabric materials, the cylindrical sample undergoes different levels of contraction, which serves as a key parameter influencing the steering ability of the soft everting robot.

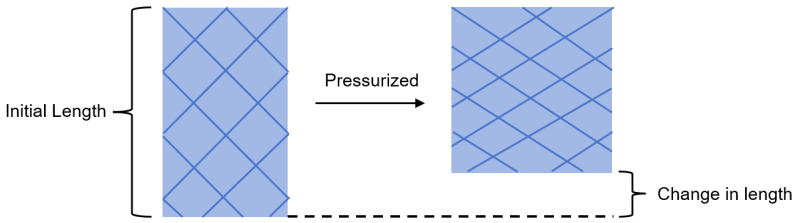

Figure 39: Contraction of cylindrical samples

This material property is being studied, quantified by the contraction ratio:

$$\text{Contraction ratio} = -\frac{\Delta L}{L_{\text{initial}}} \tag{6}$$

where ΔL is the change in length and L_{initial} is the initial length. The negative sign is to make sure that the contraction ratio for ripstop fabrics are positive.

4.3.1 Experiment Setup

Figure 40 shows the experimental setup used to test the contraction ratio of the fabric samples, with Figure 41 being the corresponding flow chart. The setup is similar to the previous one, but instead of using soft everting robots, the fabrics are held vertically in a frame, with one end fixed and the other connected to a pressure inlet. Only the growth pressure needs to be regulated, which requires one solenoid valve [SMC, ITV1050, G3/8)] controlled by the microcontroller [Teensy 4.1]. To determine the contraction ratio, the position sensor is attached at the end of the fabric, and accompanied by the field generator [Aurora, NDI], the coordinates of the end of the fabric before and after pressurization can be measured and transmitted to the console.

4.3.2 Experimental Protocol

Record the coordinates of the two ends of the fabric. Supply electric power and pressurized air into the setup, and regulate the input pressure by sending commands from the PC console. The equivalent voltage input of the solenoid valve is controlled between 0- 3.3 V, which corresponds pressure output of 0-20 kPa. The coordinate of the end of the fabric under pressurization is recorded, which can be used to compute the contraction ratio.

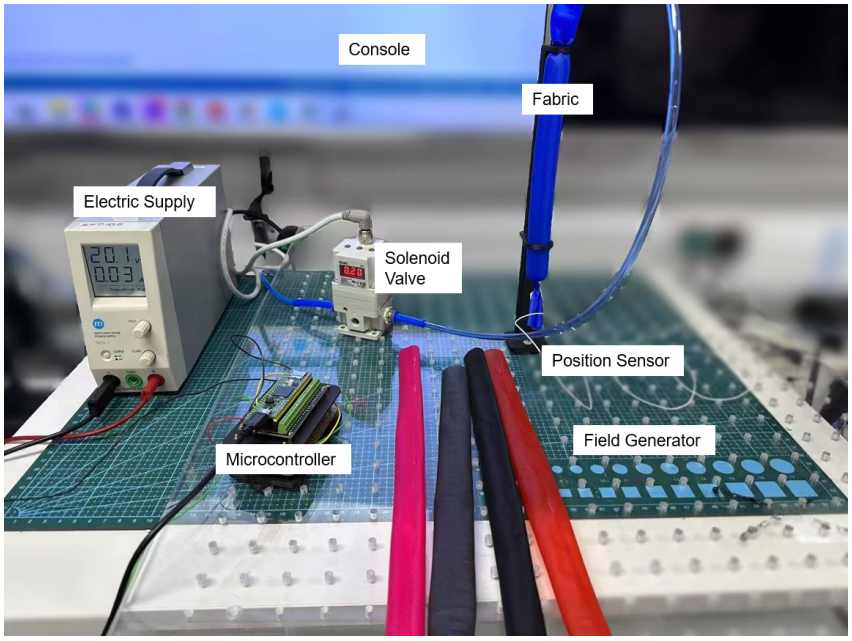

Figure 40: Experiment setup for testing contraction ratio

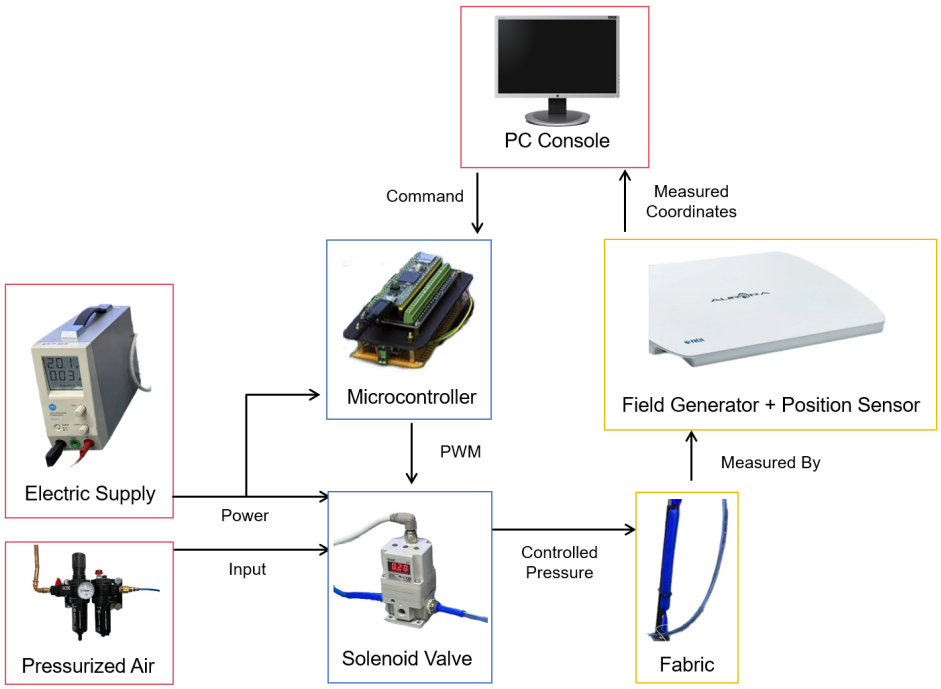

Figure 41: Flow chart for testing contraction ratio [25]

Three trials are conducted under the same condition. Subsequently, the experiment is repeated with six different fabric materials, two different sample diameters, and four different growth pressures (5 kPa, 10 kPa, 15 kPa, and 20 kPa). The contraction feature is only valid for the 45-degree grid orientation; therefore, the contraction ratio of the 0-degree orientation is not measured.

4.3.3 Results

The contraction ratio of fabric samples with a diameter of 18 mm at varying growth pressure is shown in Figure 42. For ripstop nylon fabrics, the contraction ratio increases with pressure, and the rate of change of contraction ratio decreases at higher pressure levels. Comparing the different fabrics, Fabric 3 generally exhibits the highest contraction ratio at all growth pressure levels, which is followed by Fabric 2, Fabric 5, Fabric 4 and Fabric 1. The deviation between contraction ratio is subtle at low pressure, and becomes more pronounced at higher levels of growth pressure. By contrast, unlike the ripstop nylon samples, the plastic sample shows a negative contraction ratio, indicating that the sample expands rather than contracts under pressure.

For samples with a larger diameter of 25 mm, as shown in Figure 43, the contraction ratio shows a similar pattern. Fabric 3 exhibits the largest contraction, with about 0.1 contraction ratio at 20 kPa growth pressure for both sample diameters, which is followed by Fabric 2, Fabric 5, Fabric 4, and Fabric 1, consistent with the previous result. The contraction ratio of plastic is still negative under such condition.

Referring to Section 4.2.3, the ranking of contraction ratios among different fabrics matches the ranking of steering angle of samples at high growth pressure. This implies that for sample with a grid configuration at a 45-degree angle to the growth direction at high growth pressure, contraction ratio is the predominant factor influencing the steering performance.

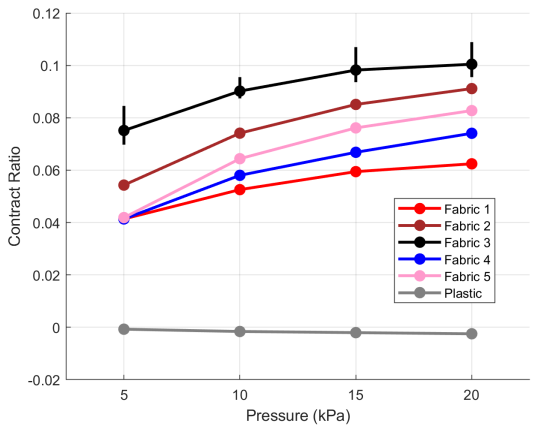

Figure 42: Contraction ratio of fabric samples with 18 mm diameter

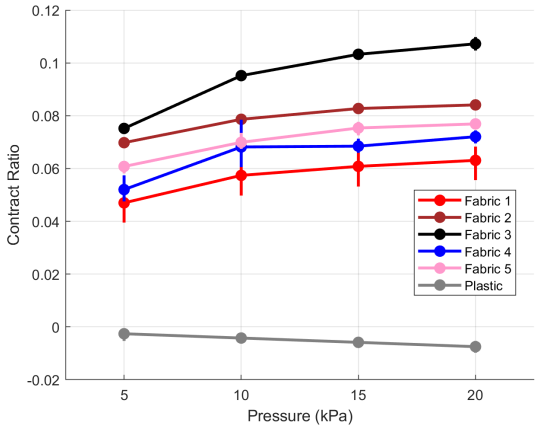

Figure 43: Contraction ratio of fabric samples with 25 mm diameter

5 Discussion

5.1 Discussion about the Result

Overall the findings confirm that key parameters, such as manipulator length, manipulator material, and fabric characteristic, have measurable effects on the steering performance of soft everting robots. Section 3.2.2 investigates the effect of manipulator lengths on steering performance. The result shows that short manipulators exhibit a small steering angle and cannot retain constant curvature, while long manipulators have poorer manoeuvrability with only a minor increase in steering angle, proving that moderate length of 105 mm has a better steering performance.

Section 3.2.3 investigates the effect of manipulator materials. It is shown that samples with Dragonskin 10 and Ecoflex 50 fails to bend the fabric at high growth pressure, as soft manipulators tend to bend internally within the fabric, which is not ideal for steering. In contrast, Dragon Skin 30 achieves insufficient steering angles under the same level of pressurisation. Dragonskin 20 has the largest steering angle, which is more preferable.

Fabric properties come in many aspects. Section 3.2.4 investigates the fabric strength, which shows that a lower fabric strength has a better performance, as long as the fabric doesn't break under pressurization. Section 4.2.3 discusses the effect of other characteristics including thickness, diameter, grid configuration and growth pressure. Overall, a higher growth pressure leads to a smaller steering angle. At low growth pressure, thickness of the fabric is the predominant factor. Thicker fabrics lead to smaller steering angle, as thick fabric is generates more blockage and requires more force to steer. At high growth pressure, grid configuration of 45-degrees to the growth direction exhibits a much larger angle when comparing with 0-degree ones. For 0-degrees ones, thickness is still the predominant factor, with buckling taking place. As for 45-degrees ones, the contraction ratio becomes the predominant factor, as discussed in Section 4.3.3, with wrinkling taking place instead.

The finite element model aligns closely with the experimental results, highlighting the reliabil-

ity of the results, as shown in Section 4.2.4. However, there are certain deviation between these two, indicating the presence of errors. For finite element analysis, considering the computational limitation, mass scaling was enabled to reduce simulation time. While mass scaling significantly improves computational efficiency, it sacrifices certain accuracy, potentially causing errors. For the experiment part, a string is used to suspend the steerable tip. This string inevitably exerts tensile force on the soft robot, causing systematic errors. This can be improved by removing the string and instead using a surface that is as smooth as possible to minimise the effect of friction on the robot.

5.2 Limitations and Future Work

Despite the insight made in this study, there are still several limitations. To begin with, the finite element model designed in this study is a over-simplified in many ways. The background weave of the fabric is considered as a homogenous material, and is not modelled as a woven structure; The inner chambers of the manipulator are typically constrained by thin internal lines to restrain any potential sideways expansions, which is not included in the simulation. These implications are imposed in the finite element model due to consideration of the computational efficiency. In future work, the accuracy of the model can be improved by using a more powerful computer capable of handling the full-resolution model without simplifications.

During the steering angle experiments, the grid configuration investigated in this study only includes 0-degree angle and 45-degrees angle, considering the fabrication time required. Samples with a wider range of grid configuration angles, such as 30-degrees, can be fabricated and tested in the future, which helps to establish a clearer relationship between grid orientation and steering performance. In addition, the steering direction is fixed for all trials. Multi-directional steering can be investigated in the future.

6 Conclusions

This report presents a comprehensive investigation into the steering performance of soft everting robots, integrating finite element simulations and experimental validation. The finite element model developed for this study successfully predicts the physical behaviours of robots, demonstrating the influence of parameters such as manipulator length, manipulator material and fabric strength, while at the same time reinforcing its applicability for future design optimisation. Experimental characterisation extends the investigation beyond the FEA, which focuses on fabric characteristics such as thickness, grid patterns, and contraction ratio. Overall, the study successfully provides practical guidance for the design of a pneumatic steering tip for soft everting robots.

7 AI-assisted Writing Declaration

In this coursework, the generative AI was used to generate LaTeX code for certain equations, which is a time-consuming task. I also used it to proofread the report, which improved sentence fluency and reduced grammatical errors.

References

[1] L. H. Blumenschein, M. M. Coad, D. A. Haggerty, A. M. Okamura, and E. W. Hawkes, "Design, modeling, control, and application of everting vine robots," *Frontiers in Robotics and AI*, vol. 7, p. 153, 2020. [Online]. Available: https://doi.org/10.3389/frobt.2020.548266

[2] J. Shi, K. Borvorntanajanya, K. Chen, E. Franco, and F. R. y Baena, "Design, control and evaluation of a novel soft everting robot for colonoscopy," 2025.

[3] K. E. Tennakoon, G. S. Subasingha, J. A. Sewwandhi, A. L. Kulasekera, and P. C. Dassanayake, "Experimental performance characterization of an underwater growing robot," in *2023 Moratuwa Engineering Research Conference (MERCon)*, 2023, pp. 620–625. [Online]. Available: https://doi.org/10.1109/MERCon60487.2023.10355439

[4] Y. Zhao, H. Huang, W. Yuan, X. Liu, and C. C. Cao, "Worm-inspired, untethered, soft crawling robots for pipe inspections," *Soft Robotics*, vol. 11, no. 4, pp. 639–649, 2024. [Online]. Available: https://doi.org/10.1089/soro.2023.0076

[5] P. Berthet-Rayne, S. M. H. Sadati, G. Petrou, N. Patel, S. Giannarou, D. R. Leff, and C. Bergeles, "Mammobot: A miniature steerable soft growing robot for early breast cancer detection," *IEEE Robotics and Automation Letters*, vol. 6, no. 3, pp. 5056–5063, 2021. [Online]. Available: https://doi.org/10.1109/LRA.2021.3068676

[6] D. Kaleel, B. Clement, and K. Althoefer, "Hydraulic volumetric soft everting vine robot steering mechanism for underwater exploration," 09 2024. [Online]. Available: https://doi.org/10.48550/arXiv.2409.16976

[7] L. T. Gan, L. H. Blumenschein, Z. Huang, A. M. Okamura, E. W. Hawkes, and J. A. Fan, "3d electromagnetic reconfiguration enabled by soft continuum robots," *IEEE Robotics and Automation Letters*, vol. 5, no. 2, pp. 1704–1711, 2020. [Online]. Available: https://doi.org/10.1109/LRA.2020.2969922

[8] P. Polygerinos, S. Lyne, Z. Wang, L. F. Nicolini, B. Mosadegh, G. M. Whitesides, and C. J. Walsh, "Design and preliminary feasibility study of a soft robotic glove for hand function assistance in stroke survivors," *IEEE Transactions on Neural Systems and Rehabilitation Engineering*, vol. 23, no. 6, pp. 958–967, 2015. [Online]. Available: https://doi.org/10.3389/fnins.2017.00547

[9] M. M. Coad, L. H. Blumenschein, S. Cutler, J. A. R. Zepeda, N. D. Naclerio, H. El-Hussieny, U. Mehmood, J.-H. Ryu, E. W. Hawkes, and A. M. Okamura, "Vine robots: Design, teleoperation, and deployment for navigation and exploration," *IEEE Robotics & Automation Magazine*, vol. 26, no. 2, pp. 120–132, 2019. [Online]. Available: https://doi.org/10.48550/arXiv.1903.00069

[10] S. M. Mirvakili and I. W. Hunter, "Artificial muscles: Mechanisms, applications, and challenges," *Advanced Materials*, vol. 30, no. 6, p. 1704407, 2018. [Online]. Available: https://doi.org/10.1002/adma.201704407

[11] A. M. Kübler, S. U. Rivera, F. B. Raphael, J. Förster, R. Siegwart, and A. M.

Okamura, “A multi-segment, soft growing robot with selective steering,” in *2023 IEEE International Conference on Soft Robotics (RoboSoft)*, 2023, pp. 1–7. [Online]. Available: https://doi.org/10.1109/RoboSoft55895.2023.10122091

[12] Y. Guo, L. Liu, Y. Liu, and J. Leng, “Review of dielectric elastomer actuators and their applications in soft robots,” *Advanced Intelligent Systems*, vol. 3, no. 5, p. 2000282, 2021. [Online]. Available: https://doi.org/10.1002/aisy.202000282

[13] T. Takahashi, K. Tadakuma, M. Watanabe, E. Takane, N. Hookabe, H. Kajiahara, T. Yamasaki, M. Konyo, and S. Tadokoro, “Eversion robotic mechanism with hydraulic skeletonto realize steering function,” *IEEE Robotics and Automation Letters*, vol. 6, no. 3, pp. 5413–5420, 2021. [Online]. Available: https://doi.org/10.1109/LRA.2021.3073653

[14] N. G. Kim, N. J. Greenidge, J. Davy, S. Park, J. H. Chandler, J.-H. Ryu, and P. Valdastri, “External steering of vine robots via magnetic actuation,” *Soft Robotics*, vol. 12, no. 2, pp. 159–170, 2025, pMID: 39288083. [Online]. Available: https://doi.org/10.1089/soro.2023.0182

[15] J. Libby, A. A. Somwanshi, F. Stancati, G. Tyagi, A. Patel, N. Bhatt, J. R. Rizzo, and S. F. Atashzar, “What happens when pneu-net soft robotic actuators get fatigued?” in *2023 International Symposium on Medical Robotics (ISMR)*. IEEE, 2023, pp. 1–6. [Online]. Available: https://doi.org/10.1109/ISMR57123.2023.10130227

[16] H. El-Hussieny, “Dynamic modelling and task-space control of vine-like soft growing robots,” in *2023 62nd Annual Conference of the Society of Instrument and Control Engineers (SICE)*, 2023, pp. 1220–1225. [Online]. Available: https://doi.org/10.23919/SICE59929.2023.10354133

[17] M. Jokar and F. Semperlotti, “Two-dimensional finite element network analysis: Formulation and static analysis of structural assemblies,” *Computers Structures*, vol. 266, p. 106784, 2022. [Online]. Available: https://www.sciencedirect.com/science/article/pii/S004579492200044X

[18] C. du Pasquier, S. Jeong, and A. M. Okamura, “Finite element modeling of pneumatic bending actuators for inflated-beam robots,” 2023, anisotropic material;Anisotropic

material model;Bending actuators;Element models;Explicit FEA;Inflated beams;Inflated-beam robot;Material modeling;Material-based;Pneumatic actuation;. [Online]. Available: http://dx.doi.org/10.48550/arXiv.2306.04048

[19] QUDT.org, "Denier - unit of linear mass density," https://qudt.org/vocab/unit/Denier.html, 2024, accessed: 2025-05-30.

[20] A. Djoumessi, N. Tagne, T. Stanislas, F. Ngapgue, and N. ebénézer, "Optimization of the young's modulus of woven composite material made by raphia vinifiera fiber/epoxy," *International Journal for Simulation and Multidisciplinary Design Optimization*, vol. 13, 10 2022. [Online]. Available: https://doi.org/10.1051/smdo/2022014

[21] W. D. Callister and D. G. Rethwisch, *Materials Science and Engineering: An Introduction*, 9th ed. John Wiley & Sons, 2013. [Online]. Available: https://ftp.idu.ac.id/wp-content/uploads/ebook/tdg/TEKNOLOGI%20REKAYASA%20MATERIAL%20PERTAHANAN/Materials%20Science%20and%20Engineering%20An%20Introduction%20by%20William%20D.%20Callister,%20Jr.,%20David%20G.%20Rethwish%20(z-lib.org).pdf

[22] L. Marechal, P. Balland, L. Lindenroth, F. Petrou, C. Kontovounisios, and F. Bello, "Toward a common framework and database of materials for soft robotics," *Soft Robotics*, vol. 8, no. 3, pp. 284–297, 2021. [Online]. Available: https://doi.org/10.1089/soro.2019.0115

[23] L. Marechal and L. Lindenroth, "Soft robotics materials database," 2024, accessed: 2025-06-02. [Online]. Available: https://soro-materials-database.onrender.com/

[24] N. Agharese and A. M. Okamura, "Configuration and fabrication of preformed vine robots," 2023. [Online]. Available: https://arxiv.org/abs/2306.01166

[25] NDI. Aurora field generators. Accessed: 2025-05-25. [Online]. Available: https://www.ndigital.com/electromagnetic-tracking-technology/aurora/aurora-field-generators/